Optimization of ECCD in high electron temperature plasma on the EAST tokamak

Hanlin WANG (王瀚林)[1,2], Xiaolan ZOU (邹晓岚)[3], Xiaojie WANG (王晓洁)[1], Yves PEYSSON[3], Miaohui LI (李妙辉)[1], Chenbin WU (吴陈斌)[1,2], Chao ZHANG (张超)[1], Fukun LIU (刘甫坤)[1] and Joan DECKER[4]

[1] Institute of Plasma Physics, Chinese Academy of Sciences, Hefei 230031, China
[2] University of Science and Technology of China, Hefei 230026, China
[3] CEA, IMFR, F-13108 Saint-Paul-Lez-Durance, France
[4] EPFL, Swiss Plasma Center, Lausanne, Switzerland

E-mail: xiao-lan.zou@cea.fr and xjiew@ipp.ac.cn

Received xxxxxx
Accepted for publication xxxxxx
Published xxxxxx

Abstract

A discharge with electron temperature up to 14 keV has been achieved on EAST. Analysis of the ECCD efficiency at high electron temperature under EAST parameter is presented by using C3PO/LUKE code. Simulation results show that the ECCD efficiency of X-mode increases with central electron temperature up to 10 keV and then starts to decrease above 10 keV. The efficiency degradation is due to the presence of the third harmonic extraordinary (X3) downshifted absorption at the low field side (LFS), even the cold resonance of X3 mode is located outside the plasma. As the electron temperature increases from 5 keV to 20 keV, the X3 absorption increases from 0.9 to 96.4%. The trapping electron effect at the LFS produces a reverse Ohkawa current. The competition between Fisch-Boozer current drive (FBCD) and the Ohkawa current drive (OKCD) result in the decrease of ECCD efficiency. ECCD efficiency optimization is achieved through two methods. One is to increase the toroidal angle, leading to that the X2 mode predominates again over X3 mode and the electron resonance domain of X2 mode is moving far from the trapped/passing boundary (TPB). The second one is to increase the magnetic field for moving away the X3 resonance layer from the plasma, hence less EC power absorbed by X3 mode.

Keywords: Current Drive, ECCD efficiency, EAST tokamak

1. Introduction

Electron cyclotron resonance heating (ECRH) [1-4] and electron cyclotron current drive (ECCD) [5-8] are the two effects produced by the interaction between electromagnetic waves in the electron cyclotron (EC) frequency or its low harmonics with plasma. Electron cyclotron systems possess a number of attractive technological features. Firstly, since the

electron cyclotron waves (ECW) propagate in vacuum, the EC launcher can be placed distant from the plasma. Secondly, the power deposition can be flexibly controlled by the toroidal magnetic field, wave frequency and antenna steering angle. Thirdly, the physics mechanism by which ECW interacts with plasma is simple, and the coupling is insensitive to the conditions at the plasma boundary. Fourthly, unlike to LHCD and ICRH, ECRH does not generate additional impurity. Finally, the EC launchers need smaller openings in the vacuum vessel as compared to other heating methods.

ECRH/ECCD is a well-established and widely used scheme for plasma localized heating and non-inductive current drive in tokamak fusion reactors [9-12]. For examples, electron heat transport has been studied [13] and the heat pinch has been calculated [14, 15] by ECRH modulation in Tore Supra, electron temperature profile stiffness has been investigated in Axially Symmetric Divertor Experiment (ASDEX) Upgrade [16], impurity transport with ECRH has been investigated in HL-2A [17]. Besides, ECRH/ECCD has been used in pre-ionization / assisted start-up [18], momentum transport / plasma rotation [19] and synergy of EC and lower-hybrid current drive [20]. Furthermore, EC power can be deposited over a wide range between the plasma centre and off-axis, ECCD can therefore be used to control the magnetohydrodynamic (MHD) instabilities [21-23], such as sawteeth control [24-26] and suppression of neoclassical tearing modes (NTM) [27-29].

Megawatt EC systems have been implemented or are planned on many fusion experiments and reactors in the last few decades, such as International Thermonuclear Experimental Reactor (ITER) [30], ASDEX Upgrade [31], JAERI Tokamak-60 Upgrade (JT-60U) [32], the Experimental Advanced Superconducting Tokamak (EAST) [33], and the China Fusion Engineering Test Reactor (CFETR) [34]. With the increasing of heating power, the electron temperature of plasma also increases. EAST achieved a discharge of electron temperature of 10 keV in the experimental campaign of 2018 [35], and achieved 14 keV in the last experimental campaign. However, ECCD is constrained by harmonic overlap at high T_e [36]. For example, the ECCD efficiency of ITER mid-plane injection is saturated at 30 keV due to the high harmonic parasitic absorption [21], the downshifted 3rd harmonic absorption at the LFS reduce the power available of 2nd harmonic as well as the driven current in JET especially at low magnetic field and high temperature [37], hence the saturation of the CD efficiency at high temperature due to increasing parasitic absorption becomes a key factor to be considered in the design of DEMO EC system [38]. Therefore, it is necessary to study the ECCD configuration optimization in high electron temperature plasma on the EAST tokamak.

Simulation and study of ECCD efficiency at high electron temperature are presented in this paper, which provide theoretical guidance for EAST tokamak experiment in the future. The paper is organized as follows. Section 2 describes the main parameters of plasma and EC system on EAST. The basic theory of ECCD and the C3PO/LUKE codes are briefly introduced in Section 3. The simulating results and discussion of ECCD efficiency at high electron temperature is presented

in section 4. The Optimization of ECCD performance by changing launch angle is addressed in section 5. Finally, a conclusion is given in Section 6.

2. Main parameters of ECRH system on EAST

High central electron temperature and high confinement long pulse steady-state discharge are the main goals of EAST operation [39]. In the experimental campaign of 2018 on EAST, more than 10 MW heating power had been injected into plasma. Under the heating of auxiliary power, the central electron temperature of the plasma reaches 10 keV [35], as shown in Figure 1. EC powers of 3 seconds pulse width were injected into the plasma center by two gyrotrons starting from 2.5 s and 3 s respectively.

EAST is a non-circular cross section, and full superconducting tokamak. The parameters of EAST are used for simulations in this paper as follows: major radius R_0 = 1.85 m, minor radius a = 0.45 m, plasma current I_P = 500 kA, aspect ratio R/a = 4.1, triangularity δ = 0.6 - 0.8 and elongation κ = 1.6 - 2 [33]. In recent experimental campaigns, B_0 is mostly operated between 2.0 T and 2.5 T, the two values of 2.2 T and 2.5 T are analyzed in this paper, where B_0 is the vacuum toroidal magnetic field in the centre at R_0.

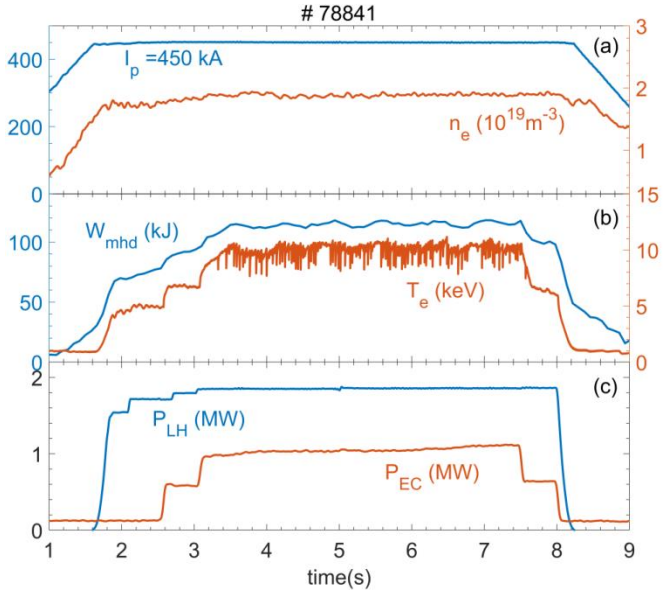

Figure 1. 10 keV electron temperature discharge in the experiment campaign of 2018 on EAST (shot No. 78841). (a) Plasma current (blue) and line-integrated electron density (red); (b) storage energy of plasma (blue) and central electron temperature (red); (c) the auxiliary heating power of low hybrid wave (blue) and ECW (red).

EC system is one of the most important plasma heating and current driver scheme on EAST, which consists of RF source, transmission line and EC launcher as shown in Figure 2. The microwave source consists of four gyrotrons with each 1 MW output power and pulse length of 1,000 seconds. The operational frequency of the gyrotrons is 140 GHz. The 4 MW power of ECW is injected into the plasma from the low field side through the horizontal port EC launcher by using the

second harmonic extraordinary (X2) mode. The EC launcher mainly consists of four pairs of focusing mirror and steering mirror. The launcher can changes the location of EC power deposition by adjusting the poloidal or toroidal angles of the steering mirror to achieve the desired physical objectives at different magnetic surfaces. The definitions of ECW poloidal angle θ and toroidal angle φ are shown as Figure 3. It should be noted that φ = 180 ° corresponds to the case where EC wave injection is perpendicular to the magnetic field, and in this case there is no ECCD. For typical B_0 = 2.5 T, ECW power is deposited on the magnetic axis when poloidal angle θ = 75 ° and toroidal angle φ = 180 °.

The relationship of wave frequency and toroidal magnetic field satisfying

$$f_{ce} = 28nB_t \tag{1}$$

where f_{ce} (GHz) is the ECW frequency, n is the electron harmonic number, B_t (T) is the magnetic field. According to equation (1), B_t = 2.5 T when f_{ce} = 140 GHz for second harmonic.

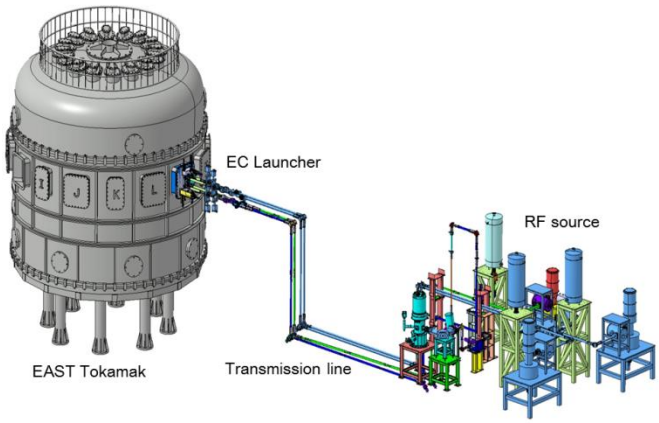

Figure 2. Layout of the EC system on EAST [33].

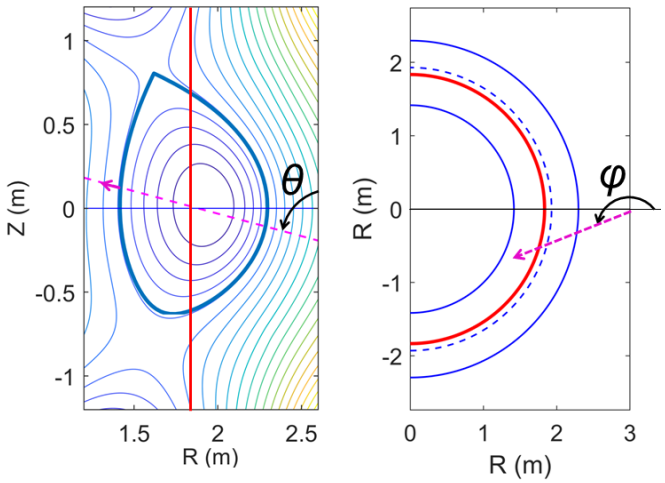

Figure 3. The definitions of poloidal angle (left) and toroidal angle (right) of ECW. The red solid lines correspond to the cold resonance layer, the pink dash lines to the ECW incident path and the blue dash line to the magnetic axis. The contour lines in the left are the plasma equilibrium shape, the blue solid lines in the right are the last closed flux surface.

All simulation is based on the plasma equilibrium and kinetic profiles of EAST baseline scenario. For simplifying the simulations, the effective charge number is set to Z_{eff} = 2. The profiles of the electron density and electron temperature are written as follows:

$$n_e(r) = (n_{e0} - n_{ea})[1 - (r/a)^{\alpha_1}]^{\beta_1} + n_{ea} \tag{2}$$

$$T_e(r) = (T_{e0} - T_{ea})[1 - (r/a)^{\alpha_2}]^{\beta_2} + T_{ea} \tag{3}$$

which are plotted in Figure 4. The central electron density n_{e0} = 5×10^{19} m^{-3}, edge density n_{ea} = 1 × 10^{19} m^{-3}. The central electron temperature T_{e0} is varying from 1 keV to 40 keV, the edge electron temperature T_{ea} is fixed at 0.1 keV. The coefficients $\alpha_1 = \alpha_2 = 3$, $\beta_1 = \beta_2 = 1$.

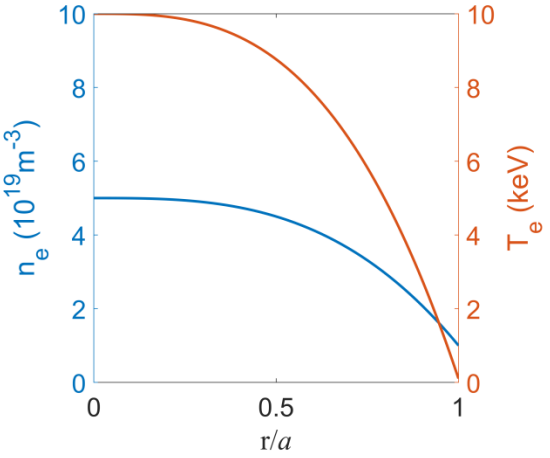

Figure 4. Electron density (blue) and electron temperature (red) profiles.

3. ECCD theory and LUKE code

ECW can be absorbed by electrons with cyclotron frequency or its low harmonics, which are satisfying the resonance condition for wave-particle interaction:

$$\omega = n\omega_{ce}/\gamma + k_{\parallel}v_{\parallel} \tag{4}$$

where ω is the frequency of ECW, n is the harmonic number, ω_{ce} is the electron cyclotron frequency, $\gamma = (1 - v^2/c^2)^{-1/2}$ is the relativistic factor, c is the velocity of light in vacuum. The first term of the right-hand side of equation (4) considers the relativistic correction of the electron mass [7]. The second term is corresponding to the Doppler shift effect, where $v_{\parallel}$ is the parallel components of the velocity of the resonant electrons, and $k_{\parallel} = \omega n_{\parallel}/c$ is the parallel component of wave vector of the ECW. The parallel refractive index $n_{\parallel}$ is positive in the direction of the magnetic field. The ECW interact with electrons that

are satisfying the electron cyclotron resonance condition, the electrons are accelerated to higher energy which result in less collision frequency in velocity space. That leads to an asymmetrical distribution of electrons in the velocity space, and form a net current.

ECCD efficiency, can be written in the form

$$\eta_{EC} = I_{EC}(A) n_e(10^{20} m^{-3}) R_0(m) / P_{EC}(W) \tag{5}$$

where I_{EC} is the total driven current, n_e is the electron density, R_0 is the major radius of the plasma, P_{EC} is the injected EC power. Definition (5) is more suitable for measuring the effect of temperature variation on I_{EC} [38].

The code used in this study is C3PO/LUKE. C3PO is a ray-tracing code which considers the weak damping approximation [40-42]. LUKE is a code for solving the three-dimensional (3D) relativistic bounce-averaged electron drift kinetic equation. [43]

The calculation processes of C3PO/LUKE are as follows. The wave propagation in the plasma is calculated by solving the ray equation using C3PO code, and the variation of EC power with trajectory is given simultaneously. Based on the wave parameters determined along each ray, the quasilinear diffusion coefficient in momentum space is evaluated self-consistently with the electron distribution function in the LUKE code, by solving simultaneously the 3D linearized relativistic bounce-averaged Fokker–Planck equation and the wave power equation until all the power carried by each ray is transferred to the particles. Then, the electron distribution function *f (r, p, ξ, t)* is obtained. Finally, the power density and driven current density are calculated.

4. ECCD efficiency of X-mode

To evaluate the ECCD efficiency in high electron temperature tokamak plasmas, simulations of ECCD efficiency versus different electron temperature are carried out as shown in Figure 5. Here, the central density $n_{e0} = 5 \times 10^{19}$ m^{-3}, poloidal angle $\theta = 75°$, toroidal angle $\varphi = 200°$, $B_0 = 2.2$ T, $P_{EC} = 1$ MW and wave frequency $f = 140$ GHz for X - mode. Theoretically, the ECCD efficiency is proportional to electron temperature[44]. However, the ECCD efficiency presented in Figure 5 is reduced after $T_{e0} > 10$ keV, even if the power absorption coefficient is almost constant.

To understand why the driven current is decreasing, the current and power density profile with different T_{e0} for X-mode ECW is presented in Figure 6(a) and 6(b), respectively. With T_{e0} increase from 5 keV to 40 keV, both the radial position of current and power density peak shift towards low field side (LFS), and the current decreases rapidly. In addition, as T_{e0} increase from 5 keV to 25 keV, the width of the power density profile increases. It can be concluded that with the increase of

electron temperature, the position of power deposition shifts from plasma centre to LFS, while the driven current keeps decreasing. Here, ρ is the normalized poloidal flux.

To analyze the reason of the power deposition shift toward LFS, the power absorbed at each minor radius is separated into two figures with different harmonic presented in Figure 7. With T_{e0} increase from 5 keV to 20 keV, the X2 component decreases gradually, while the third harmonic extraordinary (X3) component appears at the LFS and becomes to dominate. It means that the resonance condition is progressively moving from X2 mode to X3. In addition, the radial positions of power density peak shifts towards the LFS both in X2 and X3 mode, which is caused by the upshift effect ($\omega > n\omega_{ce}$) [3, 4].

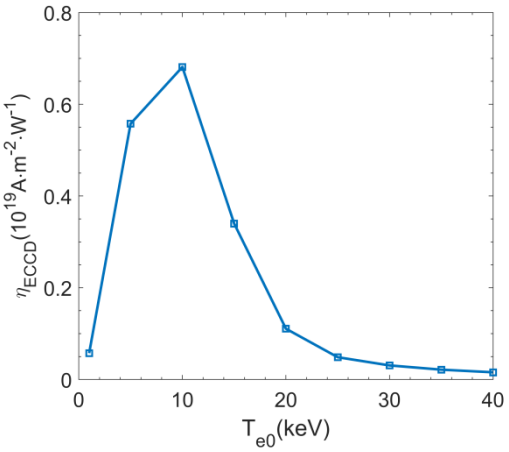

Figure 5. T_{e0} versus ECCD efficiency. Here, θ = 75 °, φ = 200 °, n_{e0} = 5 × 10^{19} m^{-3}, B_0 = 2.2 T, P_{EC} = 1 MW with X - mode.

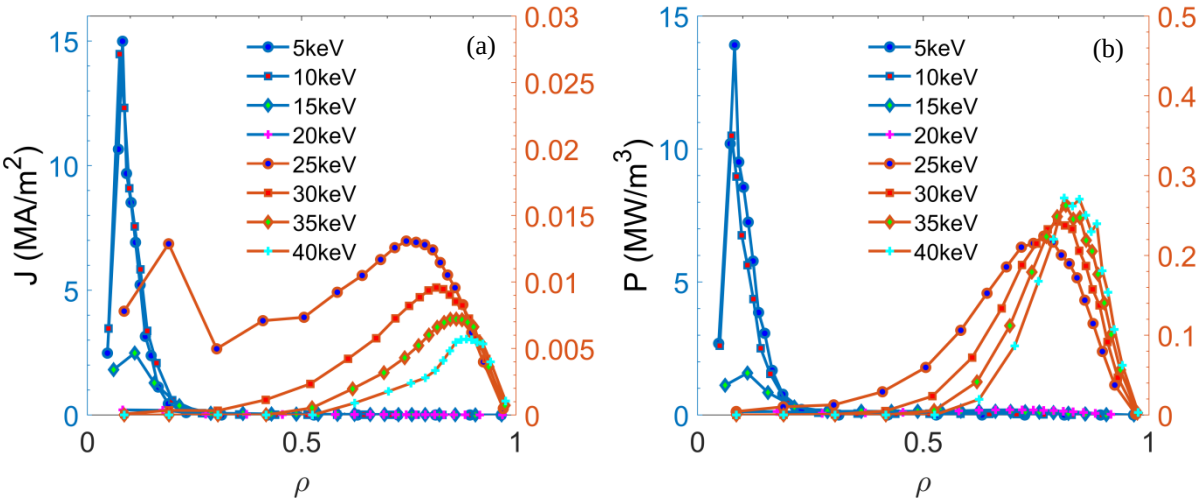

Figure 6. (a) Current and (b) power density profiles with different T_{e0}

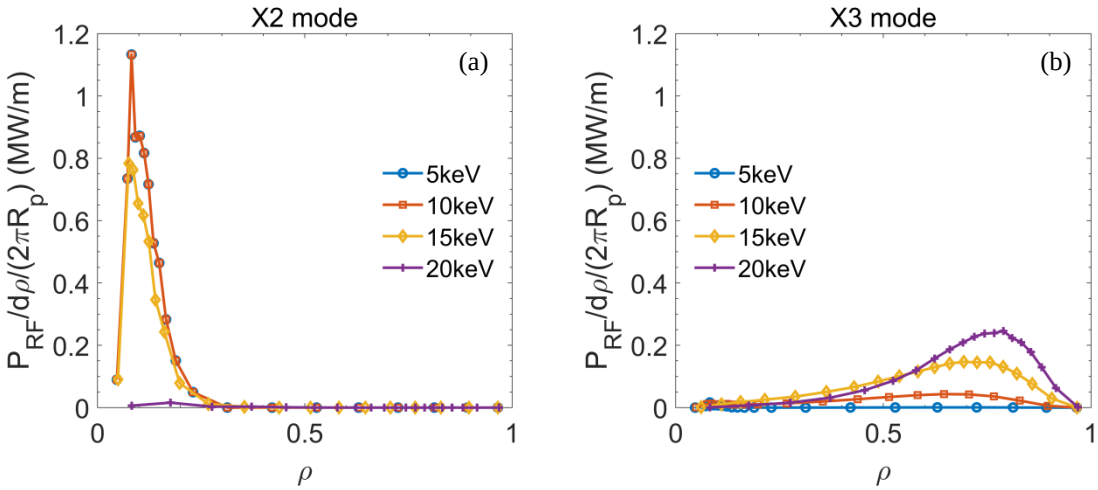

Figure 7. (a) X2 and (b) X3 component of the power absorbed at each minor radius with different T_{e0}.

Figure 8 presents the transition from second harmonic absorption to third harmonic absorption with the increase of T_{e0}. The blue and red solid lines correspond to the power absorbed by X2 and X3 component respectively, and the yellow dash line corresponds to the total absorbed power, while the injected EC power is 1 MW. When T_{e0} is less than 5 keV, almost all the EC power is absorbed by X2 component. When T_{e0} is progressively increased above 5 keV, the EC power becomes absorbed by the X3 component at the LFS, while the rest is completely absorbed by the X2 component. As the T_{e0} increases, X3 absorption turns to dominate. When T_{e0} > 25 keV, the EC power is almost completely absorbed by X3 component. During the whole process, the EC power is completely absorbed.

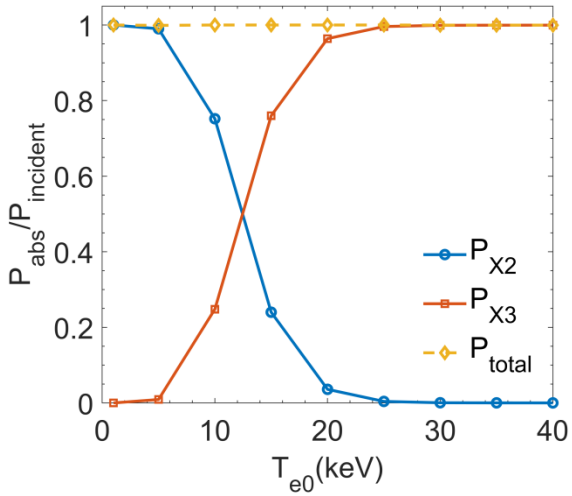

Figure 8. T_{e0} versus normalized power absorption index of X2 (blue circle), X3 (red square) component and total power (yellow diamond).

Figure 9 shows the toroidal view of ray trajectory with T_{e0} of 5 keV to 25 keV. It can be observed that when T_{e0} rises to 10 keV, X3 absorption occurs at the LFS, corresponding to the X3 component in Figure 7(b), which is the result of the downshift effect ($\omega < 3\omega_{ce}$) [3, 4, 21]. When T_{e0} is further increased to 25 keV, the EC power is completely absorbed by the X3 component.

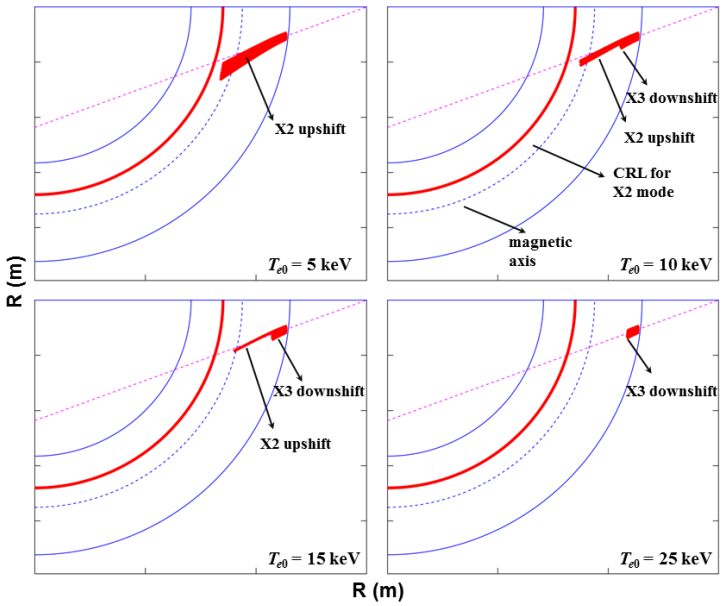

Figure 9. Ray trajectories in toroidal view with the T_{e0} increased from 5 keV to 25 keV The red solid lines correspond to the cold resonance layer of the X2 mode, the pink dash lines to the ECW incident path, the blue dash lines to the magnetic axis and the blue solid lines to the last closed flux surface.

The ray trajectory in poloidal and toroidal views at T_{e0} = 15 keV are presented in Figure 10. The cold resonance layer (CRL) of X3 mode is located at R = 2.44 m, which is theoretically outside of the plasma. However, the local resonance condition with a tail of fast electrons is more important for resonant electron. The factors affecting the local resonance condition include not only the direct thermal effect but also the relativistic mass effect. When the electron temperature is increased highly enough, the actual X3 resonance shifts to the LFS due to the downshift effect, which is illustrated by the ray trajectory in the poloidal view. Correspondingly, the actual X2 resonance is shifted due to the upshift effect, as shown with the ray trajectory near the plasma center.

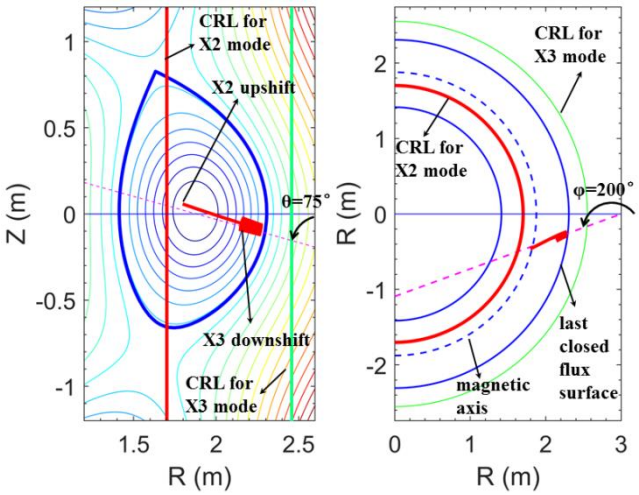

Figure 10. Ray trajectory in poloidal (left) and toroidal (right) views at T_{e0} = 15 keV. The red and green solid lines correspond to the CRL of X2 and X3 mode respectively.

ECCD contains currents generated by two different physical mechanisms, namely the Fisch-Boozer current drive (FBCD) [6] and the Ohkawa current drive (OKCD) [45], which in opposite directions[46].

The direction of toroidal magnetic field B_0 and plasma current I_p on EAST are usually set to anti-clockwise. In the steady state without ECW, electrons parallel to magnetic field are symmetrically distributed in the positive and negative directions. Once the ECW is injected clockwise as shown with the dash black and green line in Figure 11 ($n_{\parallel}$ is positive in the direction of B_0, hence here the $n_{\parallel} < 0$), the electrons with same direction are accelerated to higher energy and reduces the collision rate. Then the total velocity of electron increases, hence an anti-clockwise current (co-ECCD) is driven, found by Fisch and Boozer, as illustrated with the black solid line in Figure 11. On the other hand, due to the velocity drift caused by the ECW deposited on LFS, a part of the electrons with clockwise direction are trapped from the passing region into the trapped region. However the trapped electrons do not generate a toroidal current, thus the symmetrical distribution of electrons is lost, forming a clockwise current (counter-ECCD) namely the Ohkawa current, as shown with the green solid line.

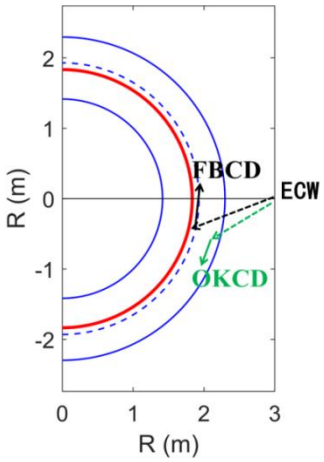

Figure 11. Schematic diagram of the direction of current driven by FBCD and OKCD mechanisms. The dash lines are the ECW incident path and the solid lines are the direction of the driven current.

Actually, these two currents can be described by a simple formula in a continuous way [47]. Based on the above physical mechanism, the decrease of driven current as the increase of electron temperature can be analysed through the electron distributions in momentum space, as illustrated in Figure 12. It can be observed that:

1) When T_{e0} = 1 keV, the power is totally absorbed by X2 component, and the resonance domain is far away from the trapped/passing boundary (TPB), there is no Ohkawa current. So there is only current driven by X2 mode FBCD mechanism.
2) When T_{e0} = 10 keV, about 25 % of EC power is absorbed by X3 component, the current driven by X3 mode is relatively weak. The rest 75% of EC power is absorbed by X2 mode near the plasma central, hence the current driven by FBCD mechanism of X2 mode (I_{OKX2}) is dominated.

3) Around T_{e0} = 15 keV, the resonance condition of X2 mode is near the plasma center, OKCD of X2 mode (I_{OKX2}) is still negligible, so the FBCD dominates in X2 mode. About 75 % power is absorbed by X3 mode, and the resonance domain is close to the TPB. The passing electrons just below the TPB will enter the trapped region after being accelerated by ECW, forming OKCD. Simultaneously, another part of electrons form FBCD. These two currents in opposite directions will counteract with each other. The total current $I_{EC} = I_{FBX2} + I_{FBX3} + I_{OKX3}$, and the $I_{OKX3} < 0$, hence the I_{EC} is reduced.

4) When T_{e0} > 25 keV, the EC power is almost completely absorbed by X3 component, the current driven by X2 absorption is negligible. The deposition of X3 mode is at the LFS, and the resonance domain is close to the TPB, so the OKCD of X3 mode is significantly increased. The total current therefore drops dramatically.

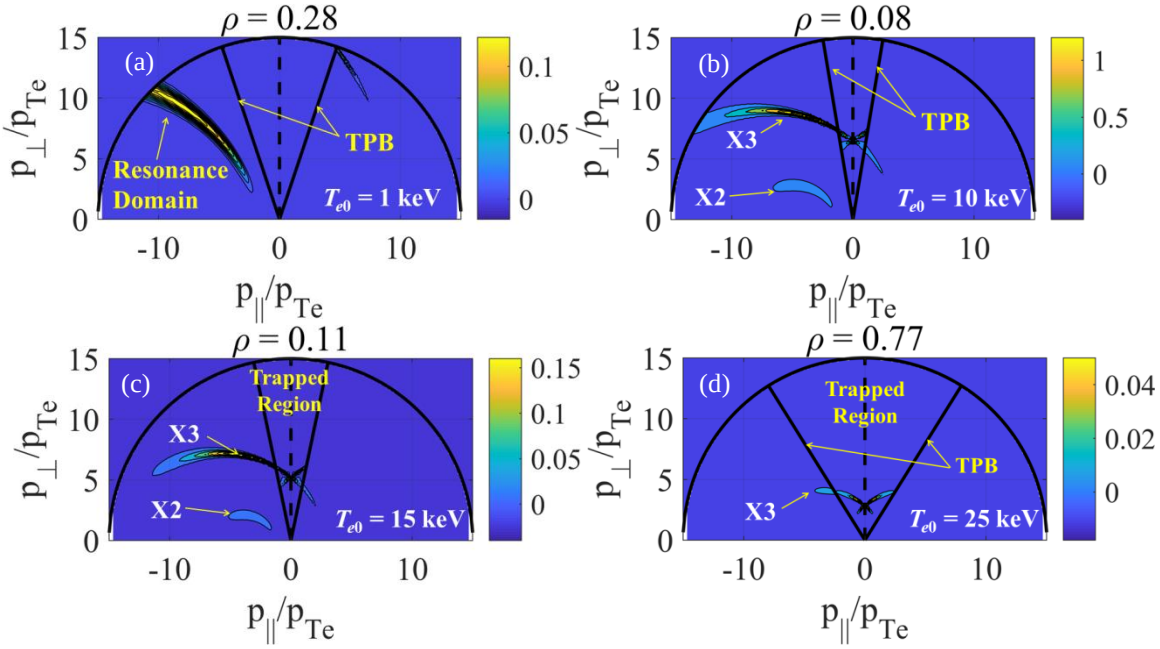

Figure 12. The electron distribution in momentum space at the radius corresponding to the maximum of the power absorption when (a) T_{e0} = 1 keV, (b) T_{e0} = 10 keV, (c) T_{e0} = 15 keV and (d) T_{e0} = 25 keV.

The sign of all parts of currents are listed in Table 1. As mentioned above, with the increase of electron temperature, the current decreases due to the X3 downshift effect and the electron trapping effect.

Table 1 The sign of each current components at different electron temperature.

T_{e0}	1 keV	10 keV	15 keV	25 keV
X2	I_{FBX2}>0	I_{FBX2}>0	I_{FBX2}>0	*N/A*
	I_{OKX2}=0	$I_{OKX2}\approx$0	$I_{OKX2}\approx$0	*N/A*
X3	*N/A*	I_{FBX3}>0	I_{FBX3}>0	I_{FBX3}>0
	N/A	I_{OKX3}<0	I_{OKX3}<0	I_{OKX3}<0
I_{EC}	I_{EC} >0 I_{FBX2} >0	I_{EC} >0 $I_{FBX2} + I_{FBX3} > \lvert I_{OKX3}\rvert$	I_{EC} >0 $I_{FBX2} + I_{FBX3} > \lvert I_{OKX3}\rvert$	I_{EC} >0 $I_{FBX3} > \lvert I_{OKX3}\rvert$

5. Optimization of the ECCD efficiency

5.1 Alter toroidal angle φ

A large number of tokamaks attempt to achieve higher ECCD efficiency to stabilize MHD modes or generate a high non-inductive toroidal current. To improve the driven current, the ECCD efficiency and power absorption coefficient at different toroidal angle φ are studied as a function of electron temperature as shown in Figure 13. And the corresponding toroidal angles are illustrated with the ray trajectory in toroidal view in Figure 14.

As mentioned above, there is no EC driven current when φ = 180 °.

Since the injection angle is almost perpendicular, the ECCD efficiency at φ = 190 ° is lower than that at φ = 200 °. The X2 absorption dominates when $T_{e0} \leq 10$ keV and the resonance condition is almost central, it is almost no OKCD effect. The X3 downshifted absorption becomes to dominate after $T_{e0} > 10$ keV, which result in the resonance condition shift towards the LFS, hence the OKCD turns to be significant. The total current $I_{EC} = I_{FBX2} + I_{FBX3} - |I_{OKX3}|$.

For φ = 210 °, with T_{e0} increases from 15 keV to 40 keV, the X3 absorption turns to dominate. The ECCD efficiency decreases after 15 keV is the result of competition between OKCD and FBCD.

When φ = 220 °, it can be observed from Figure 13(a) that, ECCD efficiency keep rising with the increase of T_{e0}, and the X3 component is negligible. The ECW are experiencing the low temperature part of the plasma. The X3 mode is very sensitive to the local electron temperature, and T_e is locally lower as φ is increasing. By increasing the toroidal angle to 220 °, X2 mode therefore predominates again over X3 mode as shown in Figure 13(c) and (d). On the other hand, the Ohkawa effect of X2 mode seems less efficient even the deposition at the LFS.

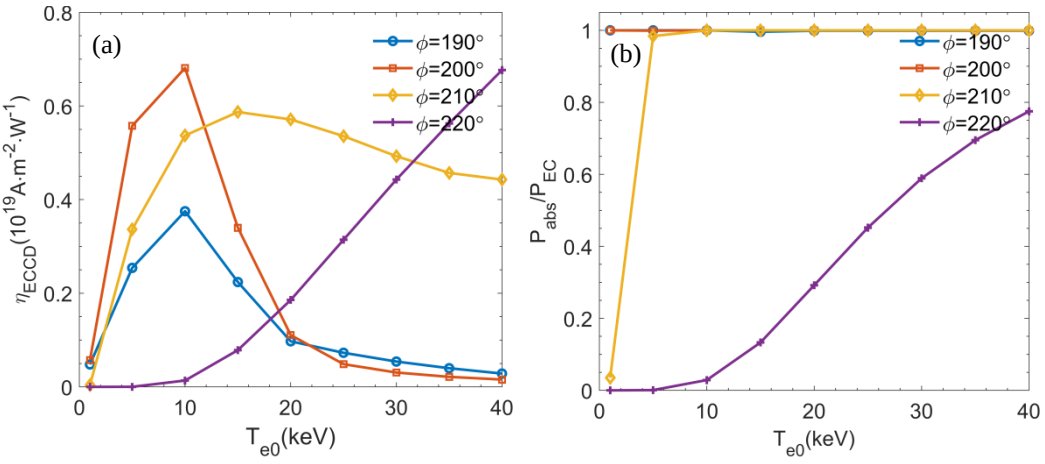

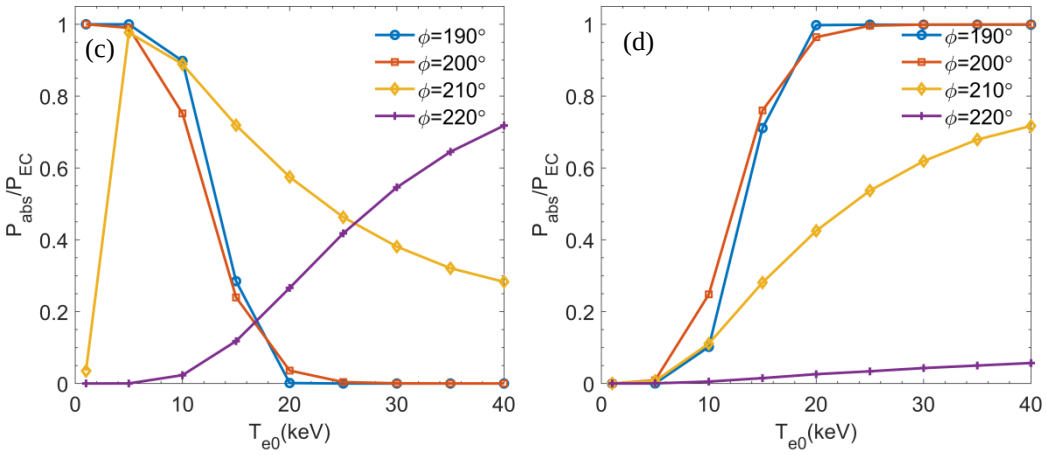

Figure 13. T_{e0} versus (a) the ECCD efficiency; and the power absorption coefficient for (b) total EC power, (c) X2 and (d) X3 component at different toroidal angle φ. Here, $\theta = 75°$, $n_{e0} = 5 \times 10^{19}$ m^{-3}, $B_0 = 2.2$ T, $P_{EC} = 1$ MW.

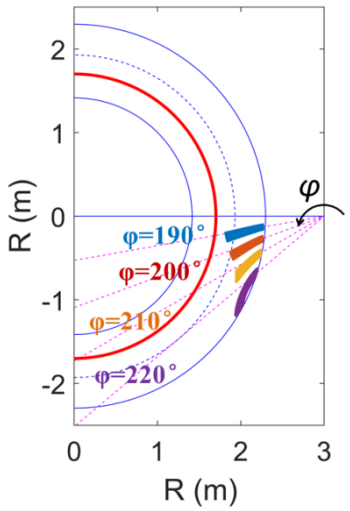

Figure 14. Ray trajectory with different toroidal angles at $T_{e0} = 6$ keV

To identify the role played by OKCD at high T_{e0} and large toroidal angle, the electron distribution in momentum space is analysed. The 2D electron distribution at $\varphi = 210°$ and $T_{e0} = 15$ keV is illustrated in Figure15. Compared with that for $\varphi = 200°$ and $T_{e0} = 15$ keV as seen in Figure 12(c), the TPB is more open so OKCD should in principle be more effective. But the resonance domain of $\varphi = 210°$ is moving towards higher parallel velocity $v_{\parallel}$ neither X2 nor X3 mode, which is more and more far from the TPB. It indicates that the FBCD effect is more dominant over the OKCD, so more EC power is coupled to the passing particles and restoring the better efficiency.

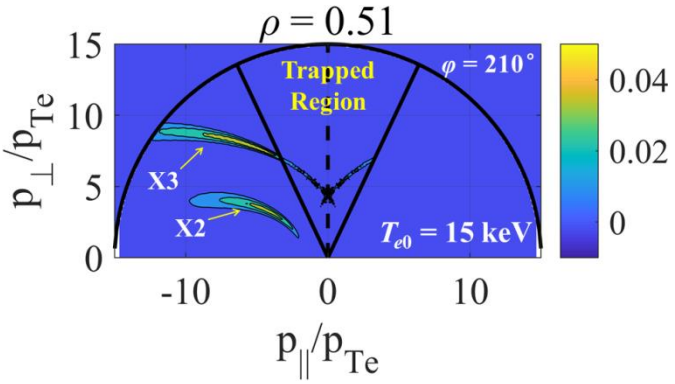

Figure 15. 2D electron distribution function at φ = 210 °and T_{e0} = 15 keV.

5.2 Alter toroidal magnetic field B_0

The EC cold resonance is located at $R_{ce} = 28nR_0(\mathrm{m})B_0(\mathrm{T})/f(\mathrm{GHz}) = R_0B_0/B_t$. In figure 16, R_{ce} is plotted versus B_0 for the second and third harmonics with f = 140 GHz. It can be observed that the EC cold resonance of 2nd harmonic shifts from the high filed side to the centre of vacuum vessel when B_0 increases from 2.2 T to 2.5 T, meanwhile the EC cold resonance of 3rd harmonic moves much far away from the plasma edge. At the same electron temperature such as Te0=15 keV, EC power absorbed by the 3rd harmonic at B_0 = 2.5 T should be less than that at 2.2 T. It indicates that the ECCD efficiency will be optimized by increasing B_0 to 2.5 T in high electron temperature plasma due to the decreasing of X3 absorption.

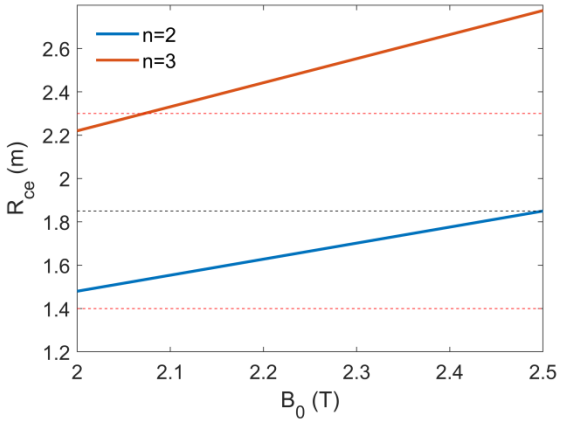

Figure 16. Major radius of EC cold resonance location as a function of the vacuum toroidal magnetic field in the centre for EC frequency f = 140 GHz. Blue and red lines refer to second and third harmonics, respectively. The horizontal black dotted line denotes the major radius of vessel centre R_0 = 1.85 m. The upper and lower red dotted lines delimit the last closed flux surface of the low and high field side, respectively.

Shear reversal, NTM stabilization and edge localized modes (ELMs) control are among the goals of EAST EC system. In the practical application of ECCD in EAST experiments, it is necessary to clarify the ECCD performance at a range of radial position and plasma parameter. Here, the ECCD efficiency and the radial location of current peak obtained by means of a wide scan of the electron temperature and toroidal angle are presented in Figure 17 (a) for 2.2T and Figure 17 (b) for 2.5T. Note that, the results presented in Figure 17 are scanned by aiming the poloidal angle to the plasma center, so the radius in

figures denotes the minimum that can be reached. The figures provide a clear view to maximize the ECCD efficiency on a specific radial position by choosing the toroidal angle and magnetic field at a given electron temperature. The overall results for both B_0 are similar, which is the ECCD efficiency behaviour with toroidal angle and electron temperature is approximately same as shown with the red solid line, although the value is different. This difference is due to the resonance condition of B_0 = 2.5 T is more outwards and the electron temperature that trigger the 3rd harmonic downshift effect are higher. For example, the radial position of MHD control (ρ ~ 0.5) can be reached at T_{e0} =10 keV or 15 keV for both B_0, even with different performances: the ECCD efficiency of B_0 = 2.2 T is about 1.2 times that of 2.5 T when T_{e0} =10 keV, but the ECCD efficiency of B_0 = 2.5 T is about 1.6 times that of 2.2 T when T_{e0} =15 keV.

The ECCD efficiency and the peak of the current density profile as a function of the electron temperature for magnetic field 2.2T and for 2.5T are shown in Figure 18 for toroidal angles from 190 to 215 °. From these plots, the following general conclusions can be drawn. The ECCD efficiency for B_0 = 2.2 T are higher than that of 2.5 T at each toroidal angle except φ = 190 and 215 ° when T_{e0} < 10 keV. And the ECCD efficiency for B_0 = 2.2 T are lower than that of 2.5 T at each toroidal angle except φ = 215 ° when T_{e0} > 15 keV. For a specific physical object such as the non-inductive toroidal current near ρ = 0.4, ECCD can be optimized by choosing B_0 = 2.2 T and φ = 210 ° if T_{e0} = 5 keV, or B_0 = 2.5 T and φ = 205 ° if T_{e0} = 15 keV.

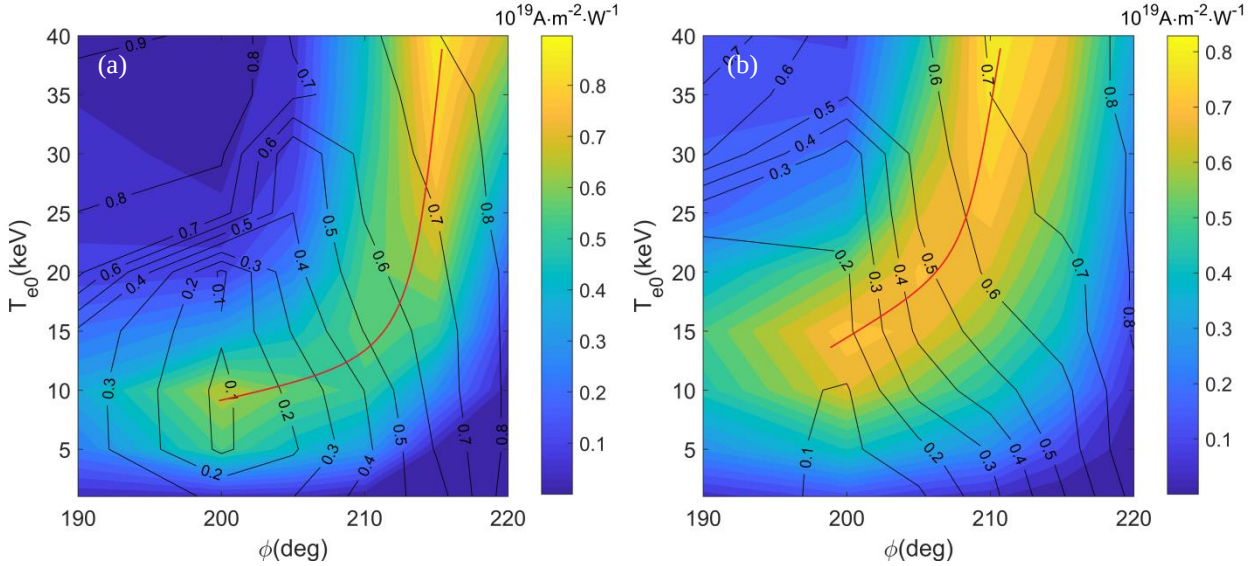

Figure 17. ECCD efficiency (colour scale) and the radial location of driven current peak (black contour lines) as a function of the toroidal angle and central electron temperature. Figures (a) and (b) refer to B_0 = 2.2T and B_0 = 2.5T, respectively. The red solid lines delight the optimal ECCD efficiency at each normalized radius.

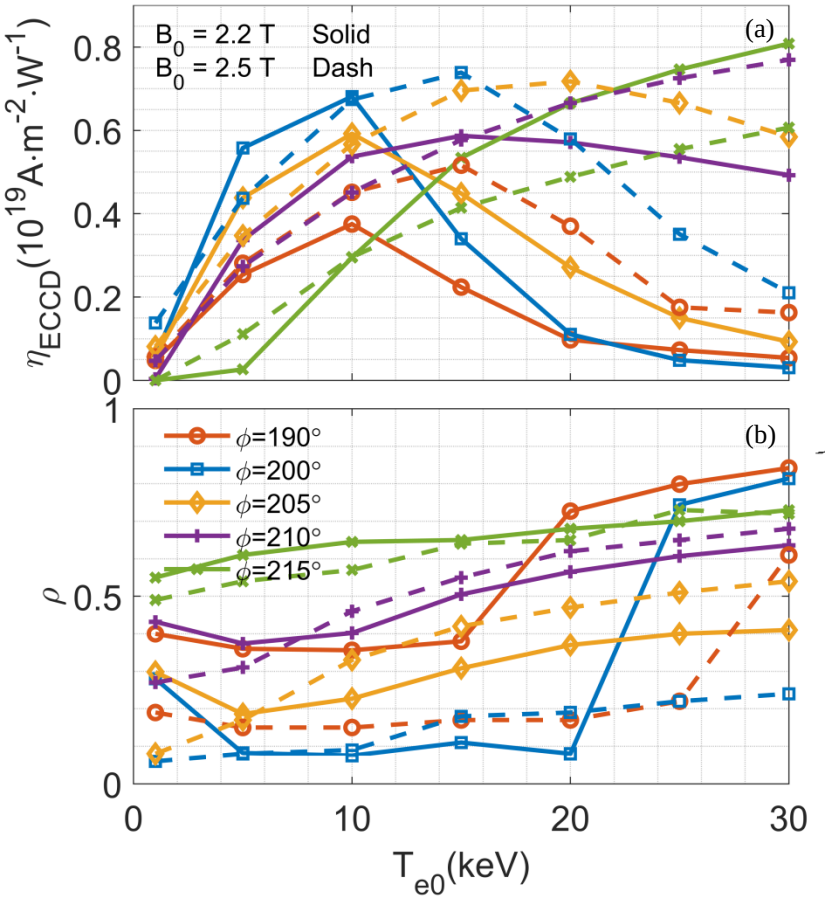

Figure 18. T_{e0} versus (a) ECCD efficiency and (b) normalized radius of current peak at the B_0 = 2.2 T (solid line) and B_0 = 2.5 T (dash line) from five toroidal angles.

6. Conclusions

EAST has achieved a discharge of electron temperature of 14 keV. The ECCD efficiency in high electron temperature plasmas is simulated. It has been found that the ECCD efficiency is greatly affected by high electron temperature, and the value of ECCD efficiency is decreased about 50% with T_{e0} increasing from 10 to 15keV. The main reasons of this degradation are as follows: 1) The X3 downshifted absorption at the low field side reducing the EC power available for 2nd harmonic. 2) The ECCD efficiency is proportional to electron temperature, the rays of X3 mode experience the low temperature part of the plasma leading to a lower ECCD efficiency. 3) The X3 absorption at the LFS produces a reverse Ohkawa current due to the electron trapping effect, which is in opposite direction to Fisch-Boozer current. The competition between these two currents leads to the decrease of the total current as well as the ECCD efficiency. Among them, the first and third reasons are the main factors.

The optimization of ECCD efficiency is achieved by decreasing the X3 absorption through two methods. One is to changing the toroidal angle φ at a fixed magnetic field in high temperature plasma. Because the X3 mode is sensitive to the local electron temperature, by increasing the toroidal angle φ to 215 °, electron temperature is locally lower as φ is increasing,

hence the X2 mode predominates again over the X3 mode. Meanwhile, the increase of φ results in the electron resonance domain of X2 mode is moving far from the TPB, it lead to the FBCD effect is more dominant again over the OKCD. The ECCD efficiency at high electron temperature is therefore optimized. The second one is to increasing magnetic field B_0 and changing toroidal angle φ appropriately. The increase of magnetic field B_0 leading to the X3 resonance region moving far away from plasma, that means the appearance of X3 downshift absorption requires a higher temperature. Thus, increasing the magnetic field B_0 to 2.5 T, the power absorbed by the X3 mode at the same temperature is reduced.

Acknowledgements

One of the authors (Hanlin Wang) would like to acknowledge the helpful suggestions by Dr. G. Giruzzi. This work is supported by National Key R&D Program of China (Nos. 2017YFE0300500, 2017YFE0300503), Comprehensive Research Facility for Fusion Technology Program of China under Contract (No. 2018-000052-73-01-001228).

References

[1] Bornatici M et al 1983 *Nucl. Fusion* **23** 1153 (DOI: https://doi.org/10.1088/0029-5515/23/9/005)
[2] Fidone I et al 1986 *Phys. Fluids* **29** 803 (DOI: https://doi.org/10.1063/1.865937)
[3] Erckmann V and Gasparino U 1994 *Plasma Phys. Control. Fusion* **36** 1869 (DOI: https://doi.org/10.1088/0741-3335/36/12/001)
[4] Prater R 2004 *Phys. Plasmas* **11** 2349 (DOI: https://doi.org/10.1063/1.1690762)
[5] Fisch N J 1978 *Phys. Rev. Lett.* **41** 873 (DOI: https://doi.org/10.1103/PhysRevLett.41.873)
[6] Fisch N J and Boozer A H 1980 *Phys. Rev. Lett.* **45** 720 (DOI: https://doi.org/10.1103/PhysRevLett.45.720)
[7] Fisch N J 1981 *Phys. Rev. A* **24** 3245 (DOI: https://doi.org/10.1103/PhysRevA.24.3245)
[8] Fisch N J 1987 *Rev. Mod. Phys.* **59** 175 (DOI: https://doi.org/10.1103/RevModPhys.59.175)
[9] Riviere A C 1986 *Plasma Phys. Control. Fusion* **28** 1263(DOI: https://doi.org/10.1088/0741-3335/28/9A/006)
[10] Prater R 1990 *J. Fusion Energy* **9** 19 (DOI: https://doi.org/10.1007/BF01057320)
[11] Lloyd B 1998 *Plasma Phys. Control. Fusion* **40** A119 (DOI: https://doi.org/10.1088/0741-3335/40/8A/010)
[12] Kirneva N A 2001 *Plasma Phys. Control. Fusion* **43** A195 (DOI: https://doi.org/10.1088/0741-3335/43/12A/314)
[13] Zou X L et al 2003 *Nucl. Fusion* **43** 1411 (DOI: https://doi.org/10.1088/0029-5515/43/11/013)
[14] Mantica P et al 2000 *Phys. Rev. Lett.* **85** 4534 (DOI: https://doi.org/10.1103/PhysRevLett.85.4534)
[15] Song S D et al 2012 *Nucl. Fusion* **52** 033006 (DOI: https://doi.org/10.1088/0029-5515/52/3/033006)
[16] Ryter F et al 2001 *Phys. Rev. Lett.* **86** 5498 (DOI: https://doi.org/10.1103/PhysRevLett.86.5498)
[17] Cui Z Y et al 2013 *Nucl. Fusion* **53** 093001 (DOI: https://doi.org/10.1088/0029-5515/53/9/093001)
[18] Seol J et al 2010 *Nucl. Fusion* **50** 105008 (DOI: https://doi.org/10.1088/0029-5515/50/10/105008)
[19] Yoshida M et al 2009 *Phys. Rev. Lett.* **103** 065003 (DOI: https://doi.org/10.1103/PhysRevLett.103.065003)
[20] Giruzzi G et al 2004 *Phys. Rev. Lett.* **93** 255002(DOI: https://doi.org/10.1103/PhysRevLett.93.255002)
[21] Harvey R W et al 1997 *Nucl. Fusion* **37** 69 (DOI: https://doi.org/10.1088/0029-5515/37/1/I06)
[22] Zohm H et al 2013 *Nucl. Fusion* **53** 073019 (DOI: https://doi.org/10.1088/0029-5515/53/7/073019)
[23] Wenninger R et al 2015 *Nucl. Fusion* **55** 063003 (DOI: https://doi.org/10.1088/0029-5515/55/6/063003)
[24] Angioni C et al 2003 *Nucl. Fusion* **43** 455 (DOI: https://doi.org/10.1088/0029-5515/43/6/308
[25] Nowak S et al 2014 *Nucl. Fusion* **54** 033003 (DOI: https://doi.org/10.1088/0029-5515/54/3/033003)
[26] Yuan Y et al 2016 *Phys. Plasmas* **23** 062503 (DOI: https://doi.org/10.1063/1.4953605)
[27] Humphreys D A et al 2006 *Phys. Plasmas* **13** 056113 (DOI: https://doi.org/10.1063/1.2173606)
[28] Lazaros A, Maraschek M and Zohm H 2007 *Phys. Plasmas* **14** 042505 (DOI: https://doi.org/10.1063/1.2720372)
[29] Wang X et al 2015 *Phys. Plasmas* **22** 022512 (DOI: https://doi.org/10.1063/1.4913352)
[30] ITER Physics Basis Editors et al 1999 *Nucl. Fusion* **39** 2137 (DOI: https://doi.org/10.1088/0029-5515/39/12/301)
[31] Leuterer F et al 2001 *Fusion Eng. Des.* **53** 485 (DOI: https://doi.org/10.1016/S0920-3796(00)00524-X)
[32] Ikeda Y et al 2001 *Fusion Eng. Des.* **53** 351 (DOI: https://doi.org/10.1016/S0920-3796(00)00511-1)

[33] Wang X et al 2015 *Fusion Eng. Des.* **96-97** 181 (DOI: https://doi.org/10.1016/j.fusengdes.2015.03.042)
[34] Wan Y et al 2017 *Nucl. Fusion* **57** 102009 (DOI: https://doi.org/10.1088/1741-4326/aa686a)
[35] Xu L et al 2020 *Nucl. Fusion* **60** 106027 (DOI: https://doi.org/10.1088/1741-4326/abadab)
[36] Smith G R, Cohen R H and Mau T K 1987 *Phys. Fluids* **30** 3633 (DOI: https://doi.org/10.1063/1.866448)
[37] Farina D and Figini L 2010 *Nuclear Fusion* **50** 095007 (DOI: https://doi.org/ 10.1088/0029-5515/50/9/095007)
[38] Poli E et al 2013 *Nucl. Fusion* **53** 013011 (DOI: https://doi.org/10.1088/0029-5515/53/1/013011)
[39] Gong X et al 2017 *Plasma Sci. Technol.* **19** 032001 (DOI: https://doi.org/10.1088/2058-6272/19/3/032001)
[40] Peysson Y and Decker J 2008 *AIP Conference Proceedings* **1069** 176 (DOI: https://doi.org/10.1063/1.3033701)
[41] Peysson Y et al 2011 *Plasma Phys. Control. Fusion* **53** 124028 (DOI: https://doi.org/ 10.1088/0741-3335/53/12/124028)
[42] Peysson Y, Decker J and Morini L 2012 *Plasma Phys. Control. Fusion* **54** 045003(DOI: https://doi.org/ 10.1088/0741-3335/54/4/045003)
[43] Peysson Y and Decker J 2017 *Fusion Sci. Technol.* **65** 22 (DOI: https://doi.org/ 10.13182/fst13-643)
[44] Brambilla M 1997 Kinetic theory of plasma waves (Oxford: Clarendon)
[45] Ohkawa T 1976 "Steady-state operation of tokamaks by r-f heating" *General Atomics Report* **GA-A13847** (San Diego, CA: General Atomics) (http://library.psfc.mit.edu/catalog/online_pubs/tech_reports/GA-A13847.pdf)
[46] Decker J 2003 *AIP Conference Proceedings* **694** 447(DOI: https://doi.org/10.1063/1.1638075)
[47] Giruzzi G 1987 *Nucl. Fusion* **27** 1934 (DOI: https://doi.org/10.1088/0029-5515/27/11/019)